Petroleum Science 21 (2024) 2520–2535

Contents lists available at ScienceDirect

Petroleum Science

journal homepage: www.keaipublishing.com/en/journals/petroleum-science

Original Paper

A semi-analytical pressure and rate transient analysis model for inner boundary and propped fractures exhibiting dynamic behavior under long-term production conditions

Lin-Song Cheng [a, *], Chong Cao [a, b, **], Quan-Yu Pan [a], Pin Jia [a], Ren-Yi Cao [a], Zhi-Kai Wang [a, c], Jun-Jie Shi [d]

[a] College of Petroleum Engineering, China University of Petroleum (Beijing), Beijing, 102249, China
[b] Sinopec Petroleum Exploration and Production Research Institute, Beijing, 100083, China
[c] CNOOC Research Institute, Beijing, 100028, China
[d] State Key Laboratory of Water Resources Protection and Utilization in Coal Mining, Beijing, 112211, China

ARTICLE INFO

Article history:
Received 10 August 2023
Received in revised form
8 April 2024
Accepted 11 April 2024
Available online 13 April 2024

Edited by Yan-Hua Sun

Keywords:
Semi-analytical model
Length shrinkage
Dynamic behavior
Boundary changes
Transient behavior

ABSTRACT

The loss of hydrocarbon production caused by the dynamic behavior of the inner boundary and propped fractures under long-term production conditions has been widely reported in recent studies. However, the quantitative relationships for the variations of the inner boundary and propped fractures have not been determined and incorporated in the semi-analytical models for the pressure and rate transient analysis. This work focuses on describing the variations of the inner boundary and propped fractures and capturing the typical characteristics from the pressure transient curves.

A generalized semi-analytical model was developed to characterize the dynamic behavior of the inner boundary and propped fractures under long-term production conditions. The pressure-dependent length shrinkage coefficients, which quantify the length changes of the inner zone and propped fractures, are modified and incorporated into this multi-zone semi-analytical model. With simultaneous numerical iterations and numerical inversions in Laplace and real-time space, the transient solutions to pressure and rate behavior are determined in just a few seconds. The dynamic behavior of the inner boundary and propped fractures on transient pressure curves is divided into five periods: fracture bilinear flow (FR1), dynamic PFs flow (FR2), inner-area linear flow (FR3), dynamic inner boundary flow (FR4), and outer-area dominated linear flow (FR5). The early hump during FR2 period and a positive upward shift during FR4 period are captured on the log-log pressure transient curves, reflecting the dynamic behavior of the inner boundary and propped fractures during the long-term production period.

The transient pressure behavior will exhibit greater positive upward trend and the flow rate will be lower with the shrinkage of the inner boundary. The pressure derivative curve will be upward earlier as the inner boundary shrinks more rapidly. The lower permeability caused by the closure of un-propped fractures in the inner zone results in greater upward in pressure derivative curves. If the permeability loss for the dynamic behavior of the inner boundary caused by the closure of un-propped fractures is neglected, the flow rate will be overestimated in the later production period.

1. Introduction

Huge-scale hydraulic fracturing of a tight reservoir may produce a significant number of fractures. Depending on proppants and fluids filled in the fractures, the fractures can be divided into propped (abbreviated, PFs) and un-propped fractures (abbreviated, UPFs) (Jia et al., 2020; Aybar et al., 2014). Recent studies indicate that the fracture closure can result in changes in physical properties

* Corresponding author.
** Corresponding author.
E-mail addresses: lscheng@cup.edu.cn (L.-S. Cheng), caochong17_rsc@163.com (C. Cao).

https://doi.org/10.1016/j.petsci.2024.04.005

and production loss (Jia et al., 2022; Pinzon et al., 2000; Sarna et al., 2014). Three separate zones (the propped fracture zone, the stimulated area, and the outer area) are usually divided from the multi-fractured horizontal wells due to the changes in physical properties (Aybar, 2014; Bello, 2009; Brown, 2009; Moussa et al., 2020). It is believed that the PFs are in the main fracture zone while the UPFs are mainly distributed in the stimulated inner zone (Yuan et al., 2015; Stalgorova and Mattar, 2013). Recently, the dynamic behavior of fractures has attracted much attention in hydrodynamics and petroleum industry (Abirifard et al., 2022; Panahi et al., 2022; Pettersson et al., 2021; Moradi and Angus, 2019; Ren et al., 2018; Shi et al., 2023). It has been reported that only a small portion of the fractures and stimulated inner area created by the hydraulic and induced fractures will take effect in the later production period (Gaddipati et al., 2020; Sen et al., 2018; Swami et al., 2017). Therefore, the changes of dynamic boundary and fracture length shrinkage caused by pressure depletion deserves attention and further research.

In recent years, laboratory and numerical methods have been conducted to study the dynamic characteristics of fracture propagation and closure (Li et al., 2022; Wu et al., 2022; Ji et al., 2020; Mustafa et al., 2018; Dahi-Taleghani, 2011; Jia et al., 2023). The flow and geo-mechanics were coupled to analyze fracture width variation (Seth et al., 2018) and production loss with the closure of propped fractures (Liu et al., 2018). Based on linear elastic fracture mechanics, the PFs closure behavior during shut-in is properly simulated in fluid and stress coupling model (Wang Q. et al., 2022). The PFs closures for both 2D and 3D fracture geometry are simulated in the dynamic fracture closure model (DFCM) to capture the large-scale fracture deformation and small-scale contact deformation due to fluid depressurization (Wang et al., 2018). Unfortunately, the computational burden caused by the large number of fracture closures limits the application of this coupled fluid-geo-mechanical model especially for the pressure transient analysis. Moreover, numerous studies of the dynamic characteristics of PFs on transient pressure behavior have been investigated (Gupta et al., 2022; Wang K. et al., 2022; Cho and Kaneko, 2004; Karma et al., 2001; Belytschko and Tabbara, 1996). The fracture closure effect was considered as the stress-dependent conductivity/permeability in the previous studies (Cho et al., 2013; Vairogs et al., 1971). The pressure-dependent permeability, a simplified mathematical expression for fracture closure, is widely incorporated into the analytical models to analyze the transient pressure behavior (Roussel and Agrawal, 2017; Mittal et al., 2015; Chipperfield et al., 2007). However, the pressure-dependent permeability fails to provide a reliable characterization of dynamic changes in fracture geometry. The stress-dependent conductivity and fracture face skin are used to describe the closure of PFs, and the signals of PFs closure are identified from the pressure transient behavior (Hernandez et al., 2023). The width changes of PFs and spontaneous imbibition are considered in history-matching approach to characterize the dynamic behavior of PFs (Cao et al., 2023; Lamidi Benson and Clarkson, 2023). The time-dependent fracture conductivity is introduced to characterize the dynamic behavior of PFs during the production stage. The greater pressure changes of the dynamic fracture conductivity is the indicator for the PFs closure (Luo et al., 2021). The PFs segments are divided into the high-conductivity and low conductivity fracture segment to evaluate the PFs closure, and the V-shape features are observed from the pressure transient analysis (Di et al., 2021). However, this two-segments splitting and time-dependent fracture conductivity are essentially the consequence of fracture closure. It cannot truly simulate the dynamic length shrinkage of PFs with the depletion of pressure. Besides, the closure behavior of water-flooding induced fracture during shut-in period on the transient pressure was also observed (Wang et al., 2019). The relationship between dynamic fracture length and pressure changes is established to describe the dynamic closure of PFs (Cao et al., 2022). Although the closure of PFs and water injection-induced fractures have been well studied, the description of dynamic behavior of inner boundary caused by the UPFs closure and the typical signals of inner boundary shrinkage from the transient pressure behavior has not been reported.

The results of the recent studies showed that UPFs distributed in the stimulated inner zone would close gradually under long-term production conditions, which could result in the loss of hydrocarbon production. The coupled hydro-mechanical model was proposed to describe the normal stress and fracture closure of the UPFs in porous media (Fabbri et al., 2021). The closure behavior of UPFs was described by the continuum constitutive model. Unfortunately, the effect of UPFs closure on transient pressure behavior has not been investigated thoroughly. The coupled flow model of fracturing fluid flow and proppant transport, proposed by Ji et al. (2019), Kamali and Ghassemi (2019), Ren et al. (2019), indicated that UPFs also have a significant contribution to the productivities. However, this numerical algorithm requires a large number of grid divisions and brings a huge computational effort, which is not suitable for the quick analysis of transient flow behavior. To assess the long-term influence of UPFs dynamic properties, the link between effective stress and permeability of UPFs was employed and implemented into the analytical model (Aybar, 2014). This simple pressure-dependent permeability equation cannot precisely represent the UPFs closure behavior. Until now, the length shrinkage of dynamic boundary and propped fracture has still not been quantitatively described and incorporated in the semi-analytical models, making it hard to capture the typical characteristics from the pressure transient curves. Above all, there is an urgent need for a semi-analytical model that can balance computational cost and characterization for the dynamic behavior of inner boundary and propped fractures.

To characterize the dynamic behavior of inner boundary and propped fractures during long-term production period, the pressure-dependent factors are proposed to quantify the length shrinkage of inner boundary and propped fractures. Then, they are incorporated into the multi-zone semi-analytical model to identify the typical features of dynamic behavior of inner boundary and propped fracture during long-term production period from transient behavior. The transient solutions of pressure and flow are derived by numerical calculations in Laplace space and real-time iterations. Finally, the sensitivity analysis of variables related to dynamic behavior of inner boundary and propped fractures (i.e., length shrinkage factor, retained coefficient and the closed-UPFs permeability) on transient responses are investigated.

The most significant contribution of this work is to characterize the length shrinkage of inner boundary and propped fractures. The typical features of dynamic inner boundary and propped fractures are identified from the transient pressure curves during the long production period. The computational cost with only a few seconds enables engineers to quickly observe typical signatures and make the estimation of dynamic behavior of inner boundary and propped fractures.

2. Description of the dynamic behavior of inner boundary and propped fractures

2.1. The closure behavior of propped and un-propped fractures

During hydraulic fracturing treatment, a large number of fluids and proppants are pumped into the wellbore. By interacting with hydraulic fractures, certain natural fractures are reactivated, and a stimulated region can be created. Hydraulic fractures are filled with

large amounts of proppants (called propped fractures, abbreviated PFs), while the activated natural fractures are usually filled with only a small number of fracturing fluids with low conductivity (also called un-propped fractures, abbreviated UPFs). The horizontal wells with multi-stages of hydraulic fracturing stimulation (MFHWs) are divided into propped fracture area, stimulated inner area distributed lots of UPFs and outer area, as shown in Fig. 1(a) and (b). As the fluids are removed from the fractures, the PFs and UPFs will gradually close. Previous studies showed that the fractures gradually closed from the tip to the center with the pressure depletion during production period after fracturing. The details can be found in Cao et al. (2022). The closure behavior of many irregular UPFs and the shrinkage of inner boundary are investigated in this paper. The stimulated inner area is regarded as a large fracture with a length of x_1, and the closure of the UPFs distributed in the stimulated inner zone is simplified as the length shrinkage of the stimulated area along the x axis, as shown in Fig. 1. Therefore, the dynamic inner boundary can be further subdivided into an open un-propped fractures inner area (open-UPFs inner area) and a closed un-propped fractures inner area (closed-UPFs inner area), while the fracture zone for the shrinkage of the propped fractures is subdivided into a closed propped fracture area (closed-PFs area) and an open propped fracture area (open-PFs area), as shown in Fig. 1(c).

In this paper, the characterization of the dynamic behavior of the inner boundary and propped fractures focuses on the length changes and permeability variations. The changes in length and permeability of the inner boundary and propped fractures are described in Fig. 2. As for the closure of PFs, the closed-PFs area with relatively lower permeability k_{FC} and the open-PFs area with fracture permeability k_F are generated with the depletion of fracture pressure ($k_{FC} < k_F$). The effect of UPF closure in the inner zone for the flow characteristics is considered as the shrinkage of the inner boundary length and a significant decrease in the inner area permeability ($k_e < k_d$). In other words, the length of the inner zone is reduced from x_1 to x_f and a decrease in permeability from k_d to k_e.

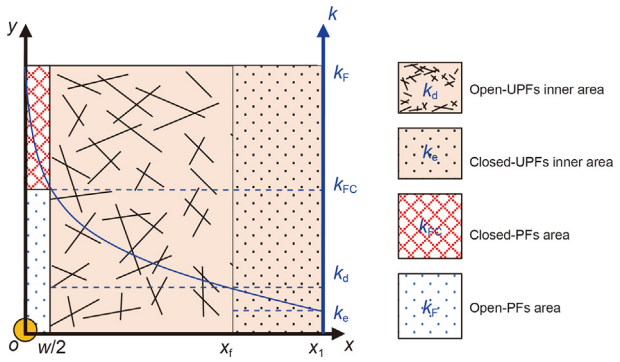

Fig. 2. Changes in physical properties caused by dynamic inner boundary and the closure of fractures.

2.2. Dynamic fracture factor

Due to the various parameter configuration, the formation may often be separated into three zones after fracturing: the PFs zone, the inner zone distributed lots of UPFs, and the outside area. It is believed that the PFs are in the main fracture zone while the complex and irregular UPFs are mainly distributed in the stimulated inner zone (Bello, 2009; Brown, 2009). It is quite challenging to provide a precise mathematical equation that captures the closure effect of UPFs. In this work, the stimulated area composed of complex and irregular UPFs is considered as a large fracture with a length of x_1. To simplify the fracture closure process and facilitate the solution, the shrinkage of UPFs is considered as the variations of inner boundary for the stimulated inner zone. It is worth noting that the shrinkage effect will be limited by the fluids and proppants in the fractures. In other words, the fracture will not entirely close even if the fracture pressure lowers to 0, and a small part of the fracture length will retain a certain conductivity. To more effectively characterize the dynamic changes of inner boundary with pressure depletion, a subsection function relation for the dynamic fracture is provided.

$$y_F(p_{wD}) = y_{F0} \cdot \sigma_F \tag{1}$$

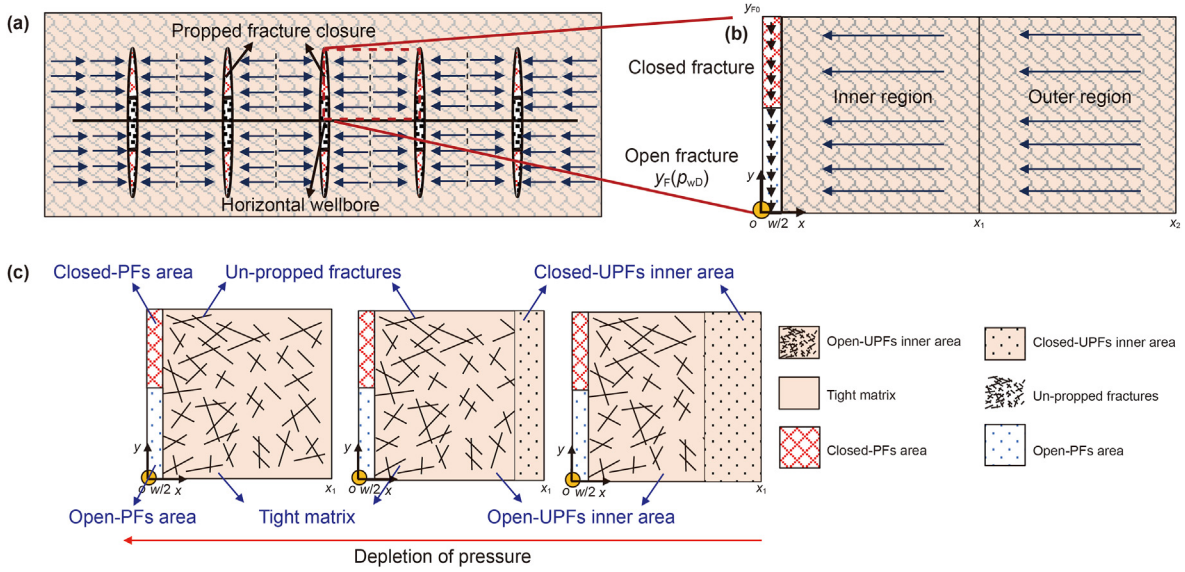

Fig. 1. Region configurations due to the dynamic shrinkage of inner boundary and the closure of fractures. (**a**) Schematic diagram of horizontal wells with multi-stages of hydraulic fracturing stimulation; (**b**) Typical three-region configurations; (**c**) Redistribution of inner area and fracture areas. The orange circle indicates the location of the wellbore.

$$\sigma_F = \max\left(1 - \frac{p_{wD} - p^0_{wD}}{\alpha}, b\right) \tag{2}$$

$$x_f(p_{wD}) = x_1 \cdot \sigma_1 \tag{3}$$

$$\sigma_1 = \max\left(1 - \frac{p_{wD} - p^0_{wD}}{\beta}, c\right) \tag{4}$$

where y_{F0} is the initial fracture length; y_F is the length of the open fracture area. The length of inner boundary shrinks from x_1 to x_f; σ_F, σ_1 are the dynamic factors of PFs and inner boundary, respectively; σ_F indicates the length ratio of open-PFs to the initial propped fractures; σ_1 indicates the extent of shrinkage along the x direction of the inner boundary; α, β are the length shrinkage factors for PFs and inner boundary, respectively, indicating how rapidly the PFs close and the inner boundary shrinks, respectively; b, c are the retained coefficients of PFs and inner boundary, respectively, suggesting the highest extent of fracture closure caused by fluid support. The retained coefficients of PFs (b) and inner boundary (c) are used to measure the retained length of the propped fractures and inner boundary when the pressure depleted.

2.3. Physical model of dynamic behavior of inner boundary and propped fractures

The region divisions and configurations of MFHWs are considered in this work (Lin et al., 2017; Wang et al., 2019). The three-zone model is considered in this work to better represent the dynamic behavior of the inner boundary caused by the UPFs closure. The reconfiguration of the whole region caused by the dynamic changes of inner boundary and propped fractures are shown in Fig. 3. To further understand how fracture closure affects transient responses, multi-zone fractured system are divided in this paper, including outer zone, open-UPFs inner zone, closed-UPFs inner zone, closed-PFs zone, and open-PFs zone. The outer area is a tight matrix, and the open-UPFs inner area and open-PFs area keep the original permeability unchanged due to the support of fluids and proppants in the fractures, and the permeability of these two areas are the permeability of the stimulated inner area (k_d) and fracture permeability (k_F), respectively. The length of closed-UPFs inner area and closed-PFs area shrink along the x and y axes, respectively, and the corresponding permeability is decreased during the pronged production period.

The assumptions for the fracture closure of PFs and UPFs are made as: (1) The UPFs are mainly distributed in the stimulated inner zone, which is consider as a large fracture with the width of x_1. Thus, the closure of UPFs can be simplified as the length shrinkage of the inner boundary. (2) For dynamic behavior of inner boundary and propped fractures during the long-term production period, the formation is divided into a multi-zone configuration with an outer zone, an open-UPFs inner zone, a closed-UPFs inner zone, a closed-PFs zone, and an open-PFs zone. (3) It is supposed that the compressibility and width of the fractures remain constant, and that two-dimensional PFs are fully penetrated and distributed uniformly along the x axis. (4) The underground fluid is regarded as a single-phase fluid with slight compressibility and constant viscosity. (5) The fluid is considered to flow perpendicular to the PFs from the outside to the inner zone.

2.4. Mathematical model

As previously stated, the PFs and UPFs will close during long-term production period and the multi-zone fractured system can be divided into outer zone, open-UPFs inner zone, closed-UPFs inner area, closed-PFs zone, and open-PFs zone. This work focuses on the shrinkage effect of inner boundary on transient pressure and rate behavior. The mathematical models of outer area, closed-UPFs inner area, open-UPFs inner area, closed-PFs area and open-PFs area are as follows. The dimensionless definition of a multi-zone dynamic fracture system can be found in Appendix A. Appendix B provides a detailed explanation of the derivation.

Outer region. Assuming closed outer boundary conditions, the unsteady fluid flow is mathematically represented as follows:

$$\begin{cases} \dfrac{\partial^2 \overline{p}_{2D}}{\partial x_D^2} - \dfrac{s}{\eta_{2D}} \overline{p}_{2D} = 0 \\ \overline{p}_{2D}(x_{1D}) = \overline{p}_{eD}(x_{1D}) \\ \left.\dfrac{\partial \overline{p}_{2D}}{\partial x_D}\right|_{x_D = x_{2D}} = 0 \end{cases} \tag{5}$$

The open-UPFs inner and outer regions are defined by the subscripts e and 2, respectively. The variable s is a Laplacian with regards to time, and the superscript "−" denotes the Laplace domain. The subscript D indicates the dimensionless variable.

Closed-UPFs inner region. The permeability hysteresis effect has been mostly reported in existing studies (Juanes et al., 2006; Mittal et al., 2015). Although the permeability (k_e) of closed-UPFs area is larger than the matrix permeability (k_2), it is lower than the permeability of the open-UPFs area (k_d), which may be the result of the partial closure of UPFs. Thus, the closed-UPFs inner zone is considered as a stimulated inner area with a permeability of the closed-UPFs area, k_e. The continuous flow rate conditions and partial differential equations (PDEs) in this closed-UPFs inner

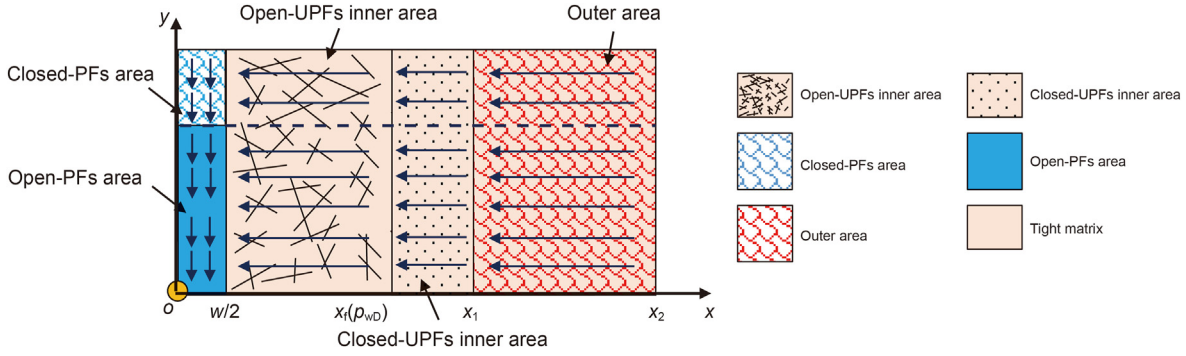

Fig. 3. The conceptual model for the shrinkage of inner area and the closure of propped fracture. w, x_1, x_2 denote the fracture width, the initial length of the inner area, and the outer area, respectively; $x_f(p_{wD})$ is the length of the open-UPFs inner zone.

region may be written as follows:

$$\begin{cases} \dfrac{\partial^2 \overline{p}_{eD}}{\partial x_D^2} - \dfrac{s}{\eta_{eD}} \overline{p}_{eD} = 0 \\ \dfrac{k_2}{\mu} \dfrac{\partial \overline{p}_{2D}}{\partial x_D}\Big|_{x_{1D}} = \dfrac{k_e}{\mu} \dfrac{\overline{p}_{eD}}{\partial x_D}\Big|_{x_{1D}} \\ \dfrac{k_d}{\mu} \dfrac{\partial \overline{p}_{dD}\left(x_{fD}\right)}{\partial x_D} = \dfrac{k_e}{\mu} \dfrac{\partial \overline{p}_{eD}\left(x_{fD}\right)}{\partial x_D} \end{cases} \tag{6}$$

where the interface between the inner zone of closed-UPFs and the outer zone is x_{1D}, while the interface between the inner zone of closed-UPFs and the inner zone of open-UPFs is x_{fD}. The subscripts 2, e, and d represent the outer region, the closed-UPFs inner region, and the open-UPFs inner region, respectively.

Open-UPFs inner region. The un-propped fracture closure behavior is simplified as the length loss of inner zone. The initial inner region gradually shrinks along the x direction, and the open-UPFs inner area can be generated. Thus, the open-UPFs inner zone has the same permeability as the original inner zone. The PDE in this open-UPFs inner region can be represented as

$$\frac{\partial^2 p_{dD}}{\partial x_D^2} - \frac{s}{\eta_{dD}} p_{dD} = 0 \tag{7}$$

At the interface x_f between the inner zones of open- and closed-UPFs, the pressure condition is continuous:

$$\overline{p}_{dD}\left(x_{fD}\right) = \overline{p}_{eD}\left(x_{fD}\right) \tag{8}$$

The interface $w/2$ between the open-UPFs inner zone, open-PFs, and the closed-PFs area is under constant pressure.

$$\overline{p}_{dD}\left(\frac{w_D}{2}\right) = \overline{p}_{FD}\left(\frac{w_D}{2}, 0 < y_D < \sigma_F\right) = \overline{p}_{FCD}\left(\frac{w_D}{2}, \sigma_F < y_D < 1\right) \tag{9}$$

where $\overline{p}_{eD}$, $\overline{p}_{dD}$, $\overline{p}_{FD}$, $\overline{p}_{FCD}$ are the pressure variables in closed-UPFs inner region, open-UPFs inner region, open-PFs region, and closed-PFs region in Laplace domains, respectively; σ_F indicates the PFs shrinkage factor, defined in Eq. (3).

Closed-PFs area. The closed-PFs permeability (k_{FC}) is lower than permeability (k_F) of PF area for the incomplete closure of PFs. Additionally, there are transient fluxes along the x direction from the open-UPFs inner area to the closed-PFs area. As a result, the PDEs with transient fluxes from the open-UPFs inner area may be expressed as

$$\frac{\partial^2 p_{FC}}{\partial y^2} + \frac{2k_d}{wk_{FC}} \frac{\partial p_d}{\partial x}\Big|_{x=w/2, y_F < y_D < y_{F0}} = \frac{1}{\eta_{FC}} \frac{\partial p_{FC}}{\partial t} \tag{10}$$

The source item from the inner region is represented by the second term on the left side of Eq. (10). Since the fracture tip is considered as closed, the boundary conditions may be written as follows:

$$\frac{\partial p_{FC}}{\partial y}\Big|_{y=y_{F0}} = 0 \tag{11}$$

The continuous conditions at the interface between the closed-PFs zone and the open-PFs zone are described as

$$p_{FC}(y = y_F) = p_F(y = y_F) \tag{12}$$

$$k_F \frac{\partial p_F}{\partial y}\Big|_{y=y_F} = k_{FC} \frac{\partial p_{FC}}{\partial y}\Big|_{y=y_F} \tag{13}$$

Eqs. (10)–(13) can be rewritten as

$$\begin{cases} \dfrac{\partial^2 p_{FCD}}{\partial y_D^2} + \dfrac{2k_d}{w_F k_{FC}} \dfrac{\partial p_{dD}}{\partial x_D}\Big|_{x_D = w_D/2, \sigma < y_D < 1} = \dfrac{1}{\eta_{FCD}} \dfrac{\partial p_{FCD}}{\partial t_D} \\ p_{FCD}(y_D = \sigma_F) = p_{FD}(y_D = \sigma_F) \\ \dfrac{\partial p_{FCD}}{\partial y_D}\Big|_{y_D=1} = 0 \end{cases} \tag{14}$$

where σ_F is the length ratio of the open-PFs (y_F) to the initial length (y_{F0}).

Open-PFs area. The PDE in the open-PFs zone is provided by considering the transient fluxes along the x direction from open-UPFs in the inner area to the open-PFs.

$$\frac{\partial^2 p_F}{\partial y^2} + \frac{2k_d}{w_F k_F} \frac{\partial p_d}{\partial x}\Big|_{x=w_F/2, 0 < y < y_F} = \frac{1}{\eta_F} \frac{\partial p_F}{\partial t} \tag{15}$$

At the bottom of the well, the constant production condition is stated as

$$\frac{\partial p_F}{\partial y}|_{y=0} = \frac{q_F \mu}{2\pi k_F wh} \tag{16}$$

The constant pressure state of the bottom of the well is represented as

$$p_F(y = 0) = p_{wf} \tag{17}$$

With Eqs. (15)–(17), the mathematical model of the open-PFs zone can be described as

$$\begin{cases} \dfrac{\partial^2 p_{FD}}{\partial y_D^2} + \dfrac{2k_d}{w_F k_F} \dfrac{\partial p_{dD}}{\partial x_D}\Big|_{x=w_D/2, 0 < y < \sigma} = \dfrac{1}{\eta_{FD}} \dfrac{\partial p_{FD}}{\partial t_D} \\ k_F \dfrac{\partial p_{FD}}{\partial y_D}\Big|_{y=\sigma} = k_{FC} \dfrac{\partial p_{FCD}}{\partial y_D}\Big|_{y=\sigma} \\ \dfrac{\partial p_{FD}}{\partial y_D}\Big|_{y_D=0} = -\dfrac{\pi}{C_{FD}} \quad \text{(CRC)} \\ \dfrac{\partial p_{FD}}{\partial y_D}\Big|_{y_D=0} = -\dfrac{\pi}{C_{FD}} q_{FD}, \ \in \overline{p}_{FD}(y_D = 0) = 1 \quad \text{(CPC)} \end{cases} \tag{18}$$

2.5. General solution for dynamic changes of inner boundary and propped fractures

The general solution of this dynamic closure of the inner boundary and PFs are derived by combining fluid flow equations in outer area, closed-UPFs inner area, open-UPFs inner area, closed-PFs area, and open-PFs area with the relevant boundary conditions, as shown in Eqs. (19) and (20). The detailed derivations for dynamic behavior of inner boundary and fracture closure are in Appendix B.

The general solution of pressure at the constant rate condition is given by

$$\overline{p}_{wD} = \frac{\pi}{F_{CD} \cdot s c_9(s)} \left(c_8(s) \sinh\left(\sigma \sqrt{c_7(s)}\right) - \cosh\left(\sigma \sqrt{c_7(s)}\right) \right) \tag{19}$$

The general solution of flow rate at the constant pressure condition is expressed as

$$\overline{q}_{\mathrm{FD}} = -\frac{C_{\mathrm{FD0}}}{\pi}\sqrt{c_7(s)}\left(-A_{\mathrm{F}}\sinh\left(\sigma\sqrt{c_7(s)}\right) + B_{\mathrm{F}}\cosh\left(\sigma\sqrt{c_7(s)}\right)\right) \tag{20}$$

where coefficients c_1–c_9 are described in Appendix B.

2.6. Computing implementation

The solutions are extremely tough to be determined in Laplace space directly because the dynamic length factors (α, β) are dependent on the pressure variations. To calculate the transient solutions with less computation cost, the synchronous iteration approach is adopted in this work. Fig. 4 depicts the precise processes for the iterative computation of pressure and flow rate. It is worth noting that the variable time step concept is utilized to accelerate the pressure iteration process allowing for the realization of the numerical inversion in Laplace domain.

3. Results

3.1. Model validation

The complex fractures can be characterized using numerical simulation methods. However, the pressure dependence (as described by Eqs. (1)–(4)) of this shrinkage effects for PFs and dynamic inner boundary makes it extremely hard to characterize especially for the commercial numerical simulation software. To verify the accuracy of the pressure and flow solutions proposed in this work, the dynamic behavior of inner boundary and propped fractures are simplified to static fractures and constant boundaries, and further compared with the pressure and flow solutions of the typical three-zone model (Stalgorova and Mattar, 2013). As shown in Eqs. (1) and (2), the dynamic fracture coefficient approaches 1 ($\sigma_{\mathrm{F}} \to 1$) when the length shrinkage factor of PFs converges to infinity ($\alpha \to \infty$), suggesting that the length of open fracture is equal to the initial fracture length ($y_{\mathrm{F}} = y_{\mathrm{F0}}$). Similarly, as the length shrinkage factor of dynamic inner boundary tends to infinity ($\beta \to \infty$), the dynamic coefficient of the inner boundary is converged to 1 ($\sigma_1 \to 1$), indicating the position of inner zone boundary is not changed. It means that the moving boundary problem evolves into a constant boundary problem. In addition, the permeability and fracture conductivity are supposed to remain constant. The permeability of closed-PFs and open-PFs are equal ($k_{\mathrm{FC}} = k_{\mathrm{F}}$), and closed-UPFs inner permeability is equal to open-UPFs inner permeability ($k_{\mathrm{e}} = k_{\mathrm{d}}$). With these parameter configurations, the solutions of pressure and flowrate without considering the dynamic behavior of the propped fractures and the inner boundary can be written as

$$\overline{p}_{\mathrm{wD}} = \frac{\pi}{C_{\mathrm{FD}} \cdot s\sqrt{c_4(s)}\tanh\left(\sqrt{c_4(s)}\right)} \tag{21}$$

$$\overline{q}_{\mathrm{FD}} = \frac{C_{\mathrm{FD}}}{\pi}\frac{\sqrt{c_4(s)}\tanh\left(\sqrt{c_4(s)}\right)}{s} \tag{22}$$

In terms of the formulation of the expression, Eqs. (21) and (22) are

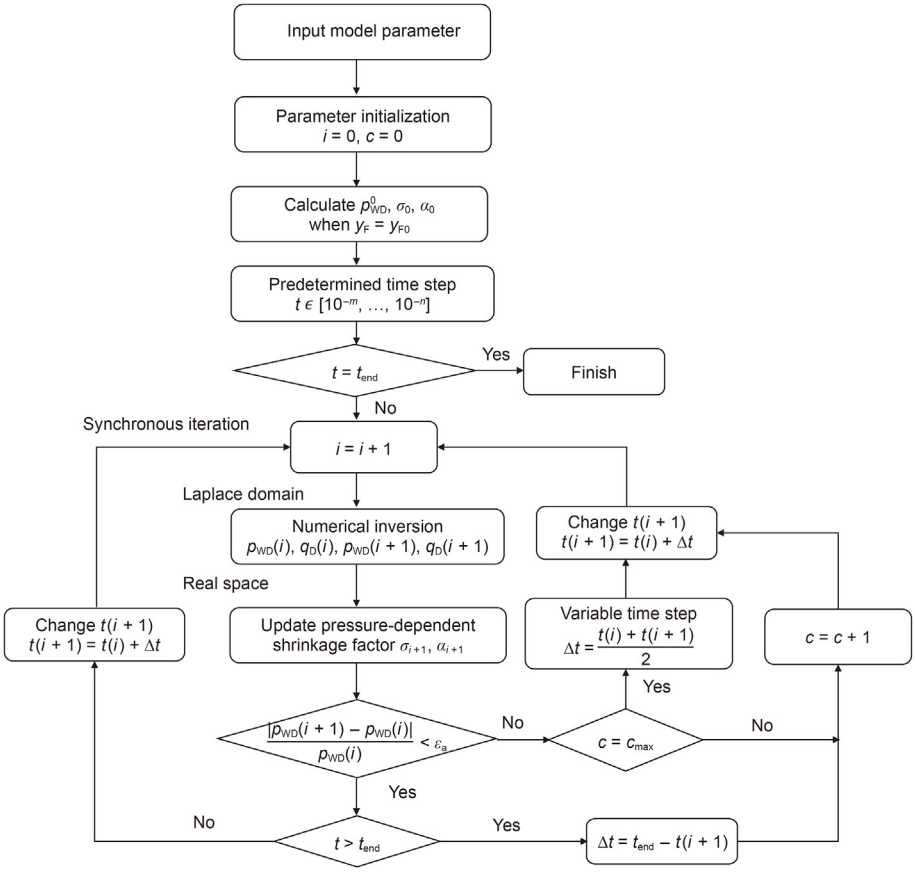

Fig. 4. Iterative procedure for the transient solutions.

consistent with those proposed by Stalgorova and Mattar (2013). The solutions of dimensionless pressure, pressure derivative, and flow rate are further calculated in this paper for the careful analysis. The parameters used for comparative analysis with "fracture-inner zone-outer zone" three-zone model proposed by Stalgorova and Mattar (2013) are presented in Table 1. The transient solutions are in perfect agreement with the observations of Stalgorova and Mattar (2013), which verifies the accuracy of this dynamic model for propped fractures and inner boundary (see Fig. 5).

3.2. Transient flow response

The dynamic behavior of inner boundary and propped fracture is considered in this study as the stimulated inner area and fractures shrink. The typical flow stages and distinctive features of dynamic inner boundary and propped fractures are captured by the pressure and rate transient analysis. The parameters for the transient analysis of the dynamic behavior are listed in Table 2. The transient flow behavior and comparative analysis between dynamic behavior and constant behavior for both inner boundary and fractures are shown in Fig. 6. The shrinkage of PFs and inner boundary causes an upward shift in the pressure and its derivative curves compared to constant fractures. The detailed analysis of flow stages and transient behavior are as follows.

Fracture bilinear flow (FR1). As shown in Fig. 6(a)—a straight line with 1/4 slope is observed in the early stages of pressure and its derivative curves. The fracture bilinear flow consists of a continuous linear flow in the open-PFs and a transient flow in the neighboring open-UPFs inner zone.

Dynamic PFs flow (FR2). The pressure derivative curve exhibits an obvious upward shift, indicating the dynamic behavior of propped fractures. The detailed analysis can be found in Cao et al. (2022). As shown in Fig. 6(b), the inflection points of the line deviating from a 1/4 slope can be used to detect the shrinkage of propped fractures. Then, the pressure derivative curve is presented a greater than unit slope, which is consistent with Wang et al. (2019). The dynamic PFs flow (FR2) occurs before the linear flow in the inner zone.

Inner-zone linear flow (FR3). The pressure derivative curve shows a half-slope straight line, which represents the fluid flows from the inner zone of open-UPFs to the PFs area (Cinco et al., 1978; El-Banbi, 1998). Compared with the constant PFs and UPFs (indicated by the red curves), an upward parallel shift of the linear flow in the inner zone occurs. It may be the result of the closure of propped fractures.

Dynamic inner boundary flow (FR4). The closure of UPFs is simplified as the length shrinkage of the inner boundary in this paper. To better capture the dynamic behavior of inner boundary, the pressure transient behavior of the dynamic PFs and UPFs with the results of constant PFs and UPFs are compared in this work. As shown in Fig. 6(b), the dynamic inner boundary is reflected on a further upward shift in the pressure derivative curves and it also presents a greater than unit slope in dynamic inner boundary flow (FR4). Like the characteristics of dynamic propped fractures, the shrinkage extent of inner boundary can be determined by deviating from the linear flow period. Moreover, this dynamic inner boundary flow (FR4) occurs between the middle and later stages of production period after the inner linear flow (FR3), which is the most obvious distinction from the dynamic behavior of propped fractures.

Outer-area dominated liner flow (FR5). The flow behavior in the late stages of the production period is governed by the boundary conditions in the outer area. The pressure derivative curve exhibits the unit slope straight line, which is the result of the closed boundary condition. The flow characteristics will change if the various outer boundary conditions are considered. It is note that the five flow stages mentioned above may not appear at the same time, depending on the parameter configurations (e.g., the permeability of open-PFs, closed-PFs, closed-UPFs inner area, open-UPFs inner area etc.).

3.3. Dynamic behavior analysis

The length shrinkage of inner boundary and propped fractures are considered in this semi-analytical model. To fully examine the effect of dynamic inner boundary and fracture closure on transient responses, four possible combined modes of PFs and UPFs are investigated, as shown in Table 2. Fig. 7(a) indicates the

Table 1
Variable configuration for the comparative investigation of the dynamic and constant fractures.

Variable	Value	
	This model	Stalgorova and Mattar, 2013
Half length of the PF y_{F0}, m	50	50
Width of propped fracture w, m	0.01	0.0
Permeability of open-PFs k_F, m^2	1×10^{-12}	1×10^{-12}
Closed-PFs permeability k_{FC}, m^2	1×10^{-12}	/
Dynamic factor of PFs σ_F	1	/
Length shrinkage factor of PFs α	Infinite	/
Retained factor of PFs b	1	/
Closed-UPFs inner permeability k_e, m^2	1×10^{-15}	1×10^{-15}
Open-UPFs inner permeability k_d, m^2	1×10^{-15}	
Dynamic factor of inner boundary σ_1	1	/
Length shrinkage factor of inner boundary β	Infinite	/
Retained coefficient of inner boundary c	1	/
Outer area permeability k_2, m^2	1×10^{-20}	1×10^{-20}
Open-PFs porosity ϕ_F	0.45	0.45
Closed-PFs porosity ϕ_{FC}	0.45	
Closed-UPFs inner zone porosity ϕ_e	0.05	0.05
Open-UPFs inner zone porosity ϕ_d	0.05	
Outer zone porosity ϕ_2	0.0064	0.0064
Open-PFs compressibility c_F, Pa^{-1}	8×10^{-10}	8×10^{-10}
Closed-PFs compressibility c_{FC}, Pa^{-1}	8×10^{-10}	
Closed-UPFs inner zone compressibility c_e, Pa^{-1}	8×10^{-11}	8×10^{-11}
Open-UPFs inner zone compressibility c_d, Pa^{-1}	8×10^{-11}	
Outer area compressibility c_2, Pa^{-1}	8×10^{-12}	8×10^{-12}

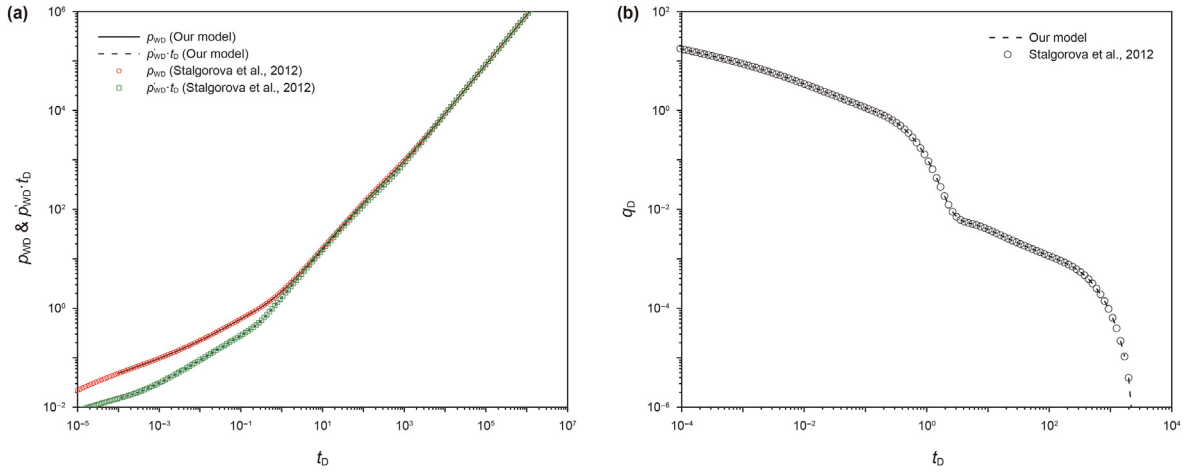

Fig. 5. Comparisons of constant fractures between this work and Stalgorova and Mattar (2013). (**a**) log-log curves for pressure transient behavior; (**b**) log-log curves for rate transient behavior.

Table 2
Parameters for rate and pressure transient analysis of propped and un-propped fractures.

Parameter	Value	Parameter	Value
Volume factor B, m^3/m^3	1	Closed-PFs compressibility c_{FC}, Pa^{-1}	8×10^{-11}
Initial reservoir pressure p_i, Pa	5.97×10^6	Open-UPFs inner compressibility c_d, Pa^{-1}	8×10^{-11}
Reservoir thickness h, m	6	Closed-UPFs inner compressibility c_e, Pa^{-1}	8×10^{-12}
Horizontal well length L, m	1850	Outer compressibility c_2, Pa^{-1}	8×10^{-12}
Number of fracturing stages, dimensionless	10	Open-PFs permeability k_F, m^2	1×10^{-12}
PFs half-length y_{F0}, m	50	Closed-PFs permeability k_{FC}, m^2	1×10^{-16}
Fluid viscosity μ, Pa s	1×10^{-3}	Open-UPFs inner permeability k_d, m^2	1×10^{-17}
Initial inner length x_1, m	46.25	Closed-UPFs inner permeability k_e, m^2	1×10^{-18}
Outer zone length x_2, m	92.5	Outer permeability k_2, m^2	1×10^{-20}
Width of fracture, m	0.01	Open-PFs porosity ϕ_F, fraction	0.45
Length shrinkage factor for PFs α	0.5	Closed-PFs porosity ϕ_{FC}, fraction	0.25
Retained factor of PFs b	0.5	Open-UPFs inner porosity ϕ_d, fraction	0.05
Length shrinkage factor of inner boundary β	0.3	Closed-UPFs inner porosity ϕ_e, fraction	0.03
Retained coefficient of inner boundary c	0.5	Outer zone porosity ϕ_2, fraction	0.0064
Open-PFs compressibility c_F, Pa^{-1}	8×10^{-10}		

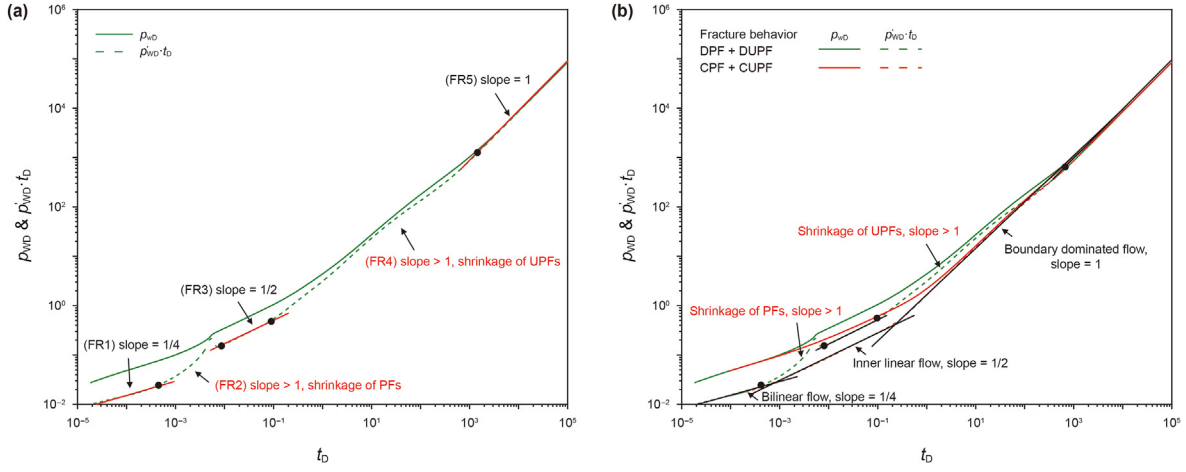

Fig. 6. Transient flow behavior (**a**) and comparative analysis (**b**) of propped and un-propped fractures with constant fractures.

comparative results of these four combined modes for PFs and UPFs. It indicates that the dynamic behavior of inner boundary and propped fractures will make the pressure and its derivative curve upward, which was also observed by van den Hoek (2003). The length loss of PFs is mainly reflected in FR2 stage, while the length loss of inner zone is mainly reflected in FR4 stage. More interestingly, the length zone of inner boundary will aggravate this upward trend especially for the FR4 period. From the transient flow rate behavior in Fig. 7(b), the length loss of the inner zone will make the flow rate decrease, especially in the middle and late stage.

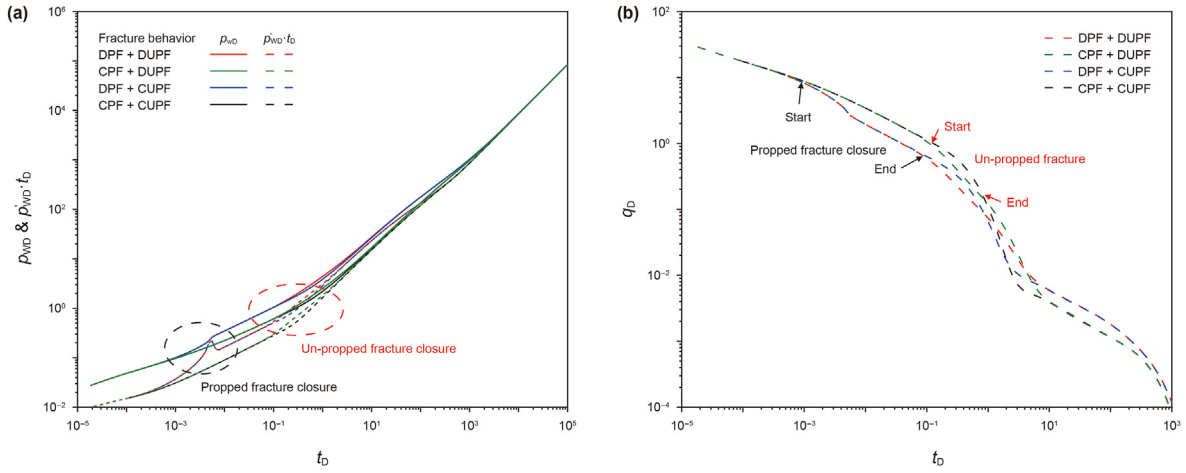

Fig. 7. The effect of dynamic behavior for the inner boundary and propped fractures on the transient responses. (**a**) Pressure transient behavior; (**b**) Rate transient behavior.

Table 3
Parameter configuration for four possible combined closure modes of PFs and UPFs.

Fracture behavior		Parameter configuration
Propped fracture	Inner boundary	
DPF	DUPF	$k_e = 0.001$, $k_d = 0.01$, $k_{FC} = 0.1$, $k_F = 1000$, $b = 0.5$, $c = 0.5$, $\beta = 0.3$, $\alpha = 0.5$
DPF	CUPF	$k_e = 0.01$, $k_d = 0.01$, $k_{FC} = 0.1$, $k_F = 1000$, $b = 0.5$, $c = 1$, $\beta = \infty$, $\alpha = 0.5$
CPF	DUPF	$k_e = 0.001$, $k_d = 0.01$, $k_{FC} = 1000$, $k_F = 1000$, $b = 1$, $c = 0.5$, $\beta = 0.3$, $\alpha = \infty$
CPF	CUPF	$k_e = 0.01$, $k_d = 0.01$, $k_{FC} = 1000$, $k_F = 1000$, $b = 1$, $c = 1$, $\beta = \infty$, $\alpha = \infty$

Notes: DPF: dynamic propped fracture; CPF: constant propped fracture, DUPF: dynamic un-propped fracture, CUPF: constant un-propped fracture.

Therefore, the flow rate in the later stage of production period will be larger if the length zone of inner boundary and propped fractures is ignored.

All the permeabilities k in Table 3 are multiplied by 10^{-15} m^2, and other parameters are dimensionless.

3.4. Sensitivity analysis

In this paper, we focus on the dynamic behavior of inner boundary and propped fractures on transient responses. Therefore, the length shrinkage coefficient of inner boundary (β), retained coefficient of inner boundary (c), and the closed-UPFs inner permeability (k_e) are investigated and the effects on the transient responses are analyzed.

3.4.1. Effect of length shrinkage factor of inner boundary

The length shrinkage factor of inner boundary (β) affects the shrinkage rate of the inner boundary, as shown in Eqs. (3) and (4). The smaller the value of β is, the faster the inner boundary shrinks along the x axis. The impact of length shrinkage coefficient of inner boundary on transient pressure responses is investigated in this work, and three cases of length shrinkage factor ($\beta = 10$, 20, 30) of inner boundary are selected, as shown in Fig. 8. In general, β has only a weak effect on the transient pressure behavior of FR4. To observe the slight changes of dynamic inner boundary on pressure derivative curves in FR4 stage, a magnified partial view is shown in the bottom of the right side. It indicates that the pressure derivative curve will be upward earlier as the inner boundary shrinks more rapidly with the decrease of β.

3.4.2. Effect of the retained coefficient of inner boundary

Due to the supporting of fluids and proppants, the fractures will remain a certain conductivity with pressure depletion. As shown in Eq. (4), the retained coefficient c is used to measure the retained length of the inner boundary when the pressure depleted. If c is equal to 0.8, it means that 20% of the inner boundary shrinks along the x axis with the closed-UPFs inner permeability (k_e) while the remaining 80% of the inner boundary remains initial inner zone permeability (k_d). Essentially, a smaller c means a larger length shrinkage of the inner boundary, resulting in a smaller length of the open-UPFs inner zone. The effect of various retained UPFs

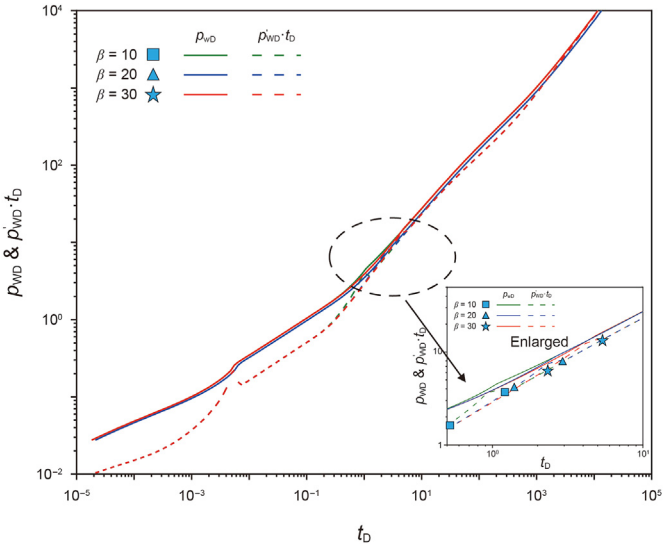

Fig. 8. The impact of length shrinkage coefficient of inner boundary on pressure transient responses.

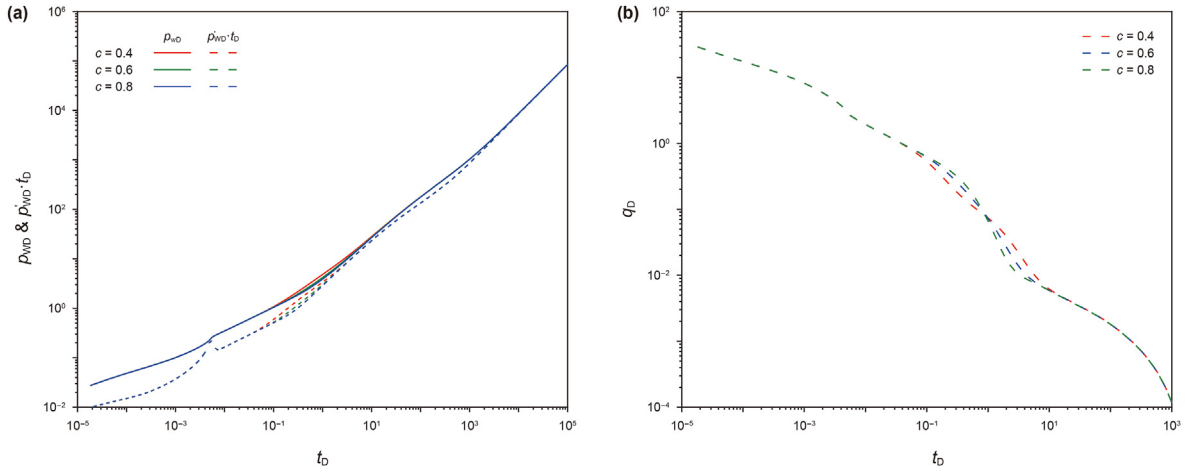

Fig. 9. The impacts of retained coefficient of UPFs.

coefficients ($c = 0.4, 0.6, 0.8$) on the transient behavior was investigated in this paper. As shown in Fig. 9, the lower flow rate and larger positive upward of pressure transient curves are observed when the retained coefficient c decreases. In other words, the transient pressure behavior will exhibit a greater positive upward trend and the flow rate will be lower with the shrinkage of the inner boundary. Therefore, the flow rate will be overestimated if the dynamic behavior of inner boundary is not taken into account, particularly in the latter production period.

3.4.3. *Effect of the closed-UPFs inner-zone permeability*

The impacts of permeability in closed-UPFs inner zone ($k_e = (0.00005–0.01) \times 10^{-15}$ m^2) on transient behavior is analyzed with the length loss of inner zone, and it has been compared with the results of constant inner boundary. As shown in Fig. 10, the transient behavior in pressure curves become more upward with the decrease of k_e, which is caused by the shrinkage of inner boundary in the stimulated inner area. It means that the lower permeability caused by the closure of un-propped fractures in inner zone results in greater upward in pressure derivative curves. From the transient flow rate in Fig. 11, the lower permeability in the closed-UPFs inner zone leads to the lower flow rate. Compared with the results of constant inner boundary, there will be a large deviation if the permeability loss in the stimulated inner area caused by the shrinkage of inner boundary is neglected, especially when the permeability in the inner area is extremely lower.

4. Discussion

As mentioned in the model assumptions, it is assumed that the UPFs are mainly distributed in the stimulated inner area, and the inner zone is considered as a large fracture with the width of x_1, and thus the closure of UPFs is simplified as the length shrinkage of inner boundary. If the length of UPFs can be accurately described in mathematical models in the near future, the length shrinkage of UPFs will be more accurately analyzed. Moreover, this paper only analyzes the case of higher permeability of closed-PFs and closed-UPFs inner zone. When the permeability of the closed-UPFs inner zone is close to the permeability of outer zone ($k_e = k_2$), the closed-UPFs inner zone will merge with the outer zone, as shown in Fig. 12(a). When the permeability of the closed-PFs zone is lower

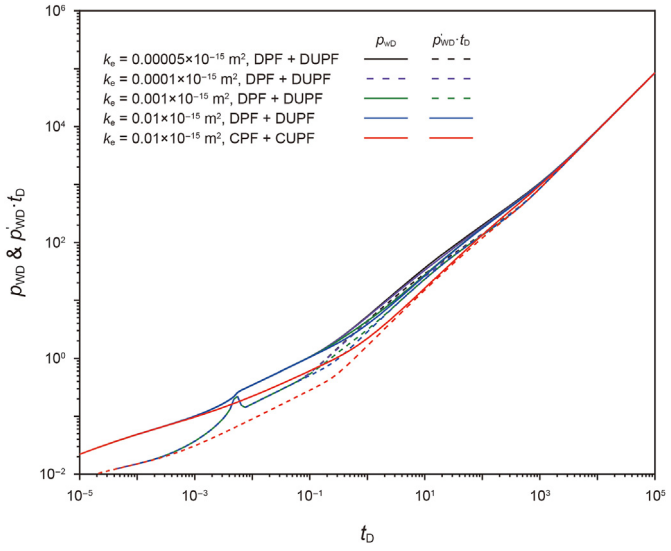

Fig. 10. The impacts of permeability in the closed-UPFs inner zone on pressure transient responses.

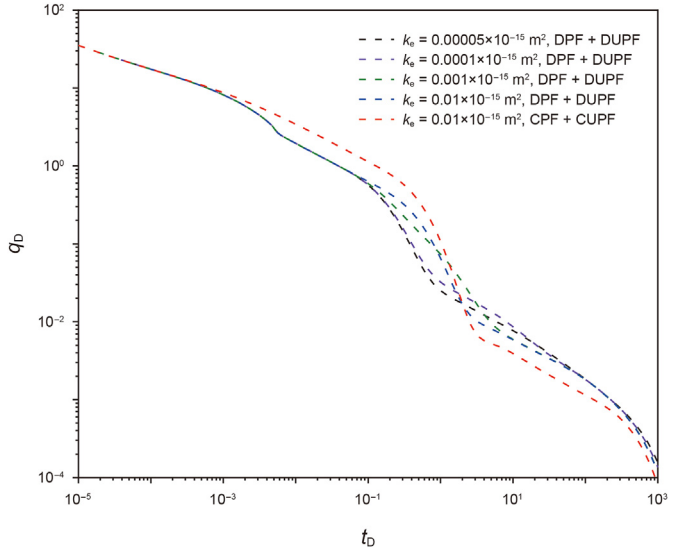

Fig. 11. The impacts of permeability in the closed-UPFs inner zone on rate transient responses.

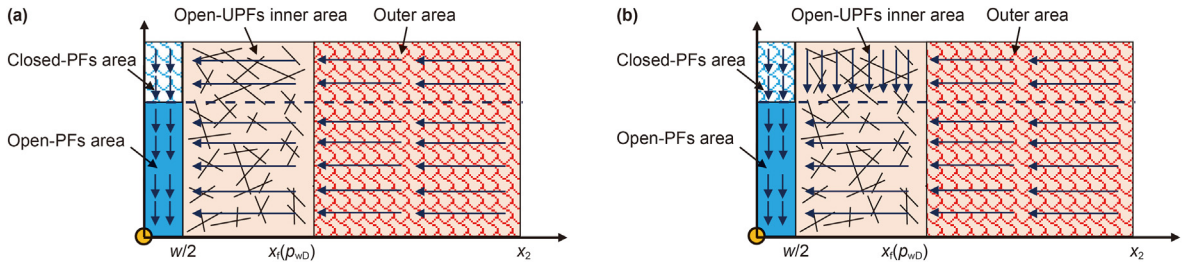

Fig. 12. Two fracture closure models for further research. (**a**) $k_e = k_2$; (**b**) $k_d < k_{FC}$.

than that of open-UPFs inner area ($k_d < k_{FC}$), the fluids in the open-UPFs inner zone will be diverted to the bottom of the open-UPFs inner zone rather than flowing into the closed-PFs zone., as shown in Fig. 12(b). These two potential possibilities are proposed for additional research in the near future.

5. Conclusions

The dynamic behavior of inner boundary and propped fractures are captured, and the typical features are identified from the transient behavior during the long-term production period. The length variations of the inner boundary and propped fractures were quantitatively characterized using the pressure-dependent length shrinkage factors. By using simultaneous numerical iterations in real space and numerical inversion in Laplace space, the transient pressure and flow solutions are obtained in a couple of seconds. The semi-analytical model of dynamical changes of inner boundary and fracture closure allows for the following conclusions.

(1) The semi-analytical model with dynamic behavior of inner boundary and propped fractures is represented by five flow phases: fracture bilinear flow (FR1), dynamic propped-fracture flow (FR2), inner area linear flow (FR3), dynamic inner boundary flow (FR4), and outer-area dominated linear flow (FR5).
(2) The propped fracture closure and dynamic inner boundary are captured by the obvious positive upward shift of the FR2 and FR4 periods, respectively. More specifically, both of the pressure derivative curves exhibit a greater than unit slope. When compared to constant fractures, the closure of PFs and shrinkage of inner boundary result in the positive upward trend on transient pressure curves. More interestingly, the dynamic behavior of inner boundary will exacerbate this upward trend especially for FR4.
(3) The shrinkage coefficient β of inner boundary mainly affects the shrinkage rate for the inner boundary. The pressure derivative curve will be upwards earlier at smaller β values due to the rapid shrinkage of inner boundary. As the retained coefficient c decreases, the pressure derivative indicates a greater positive upward trend and the flow rate in the log-log plot is lower.
(4) The lower permeability in the closed-UPFs inner zone leads to greater upward trend in pressure derivative and lower flow rates, which are attributed to the shrinkage of inner boundary in the stimulated inner zone. If the permeability loss in the stimulated inner region is neglected, especially when the permeability of the inner region is relatively lower, the flow rate will be exaggerated in the later pumping period.

Declaration of interest statement

We declare that we have no financial and personal relationships with other people or organizations that can inappropriately influence our work, there is no professional or other personal interest of any nature or kind in any production, service and or company that could be construed as influencing the position presented in, or the manuscript entitled.

CRediT authorship contribution statement

Lin-Song Cheng: Supervision, Project administration, Conceptualization. **Chong Cao:** Writing – original draft, Software, Investigation. **Quan-Yu Pan:** Writing – review & editing, Formal analysis. **Pin Jia:** Writing – review & editing, Methodology. **Ren-Yi Cao:** Writing – review & editing. **Zhi-Kai Wang:** Validation, Formal analysis. **Jun-Jie Shi:** Writing – review & editing.

Acknowledgments

We appreciate the financial funding of National Natural Science Foundation of China (No. 52004307), China National Petroleum Corporation (No. ZLZX2020-02-04), and the Science Foundation of China University of Petroleum, Beijing (No. 2462018YJRC015).

Appendix A. Dimensionless definition of a multi-zone dynamic fracture system (PFs and UPFs)

Dimensionless pressure under constant flow-rate condition is

$$p_{jD} = \frac{2\pi k_d h\left(p_i - p_j\right)}{q_F \mu B} \tag{A.1}$$

Dimensionless pressure under constant pressure condition is

$$p_{jD} = \frac{p_i - p_j}{p_i - p_{wf}} \tag{A.2}$$

Dimensionless flow rate under constant rate condition is

$$q_{FD} = \frac{q_F}{q_w} \tag{A.3}$$

Dimensionless flow rate under constant bottomhole pressure condition is

$$q_{FD} = \frac{q_F(t)\mu B}{2\pi k_d h\left(p_i - p_{wf}\right)} \tag{A.4}$$

The dimensionless time is

$$t_D = \left(\frac{k_d}{\phi_d \mu c_{td}}\right)\frac{t}{y_{F0}^2} \tag{A.5}$$

Dimensionless conductivity of open-PFs and closed-PFs is

$$C_{FD}=\frac{k_F w}{k_d y_{F0}} \tag{A.6}$$

$$C_{FCD}=\frac{w k_{FC}}{y_{F0} k_d} \tag{A.7}$$

Dimensionless diffusivity of open-PFs, closed-PFs, open-UPFs, and closed-UPFs is

$$\eta_{FD}=\frac{\eta_F}{\eta_d} \tag{A.8}$$

$$\eta_{FCD}=\frac{\eta_{FC}}{\eta_d} \tag{A.9}$$

$$\eta_{dD}=\frac{\eta_d}{\eta_d}=1 \tag{A.10}$$

$$\eta_{eD}=\frac{\eta_e}{\eta_d} \tag{A.11}$$

Permeability ratio of the propped fracture is

$$k_{FCD}=\frac{k_{FC}}{k_F} \tag{A.12}$$

Other dimensionless quantities are defined as

$$y_D=\frac{y}{y_{F0}} \tag{A.13}$$

$$x_{fD}=\frac{x_f}{y_{F0}} \tag{A.14}$$

$$x_{2D}=\frac{x_2}{y_{F0}} \tag{A.15}$$

Appendix B. Detailed derivation for the multi-zone dynamic fracture system (PFs and UPFs)

B.1 Outer area

The typical form of the subsurface fluid flow is expressed mathematically as follows:

$$\frac{\partial^2 p_2}{\partial x^2}=\frac{\phi_2 c_{t2}\mu}{k_2}\frac{\partial p_2}{\partial t} \tag{B.1}$$

The pressure at boundary between the closed-inner UPFs and outside areas is continuous.

$$p_e(x_1)=p_2(x_1) \tag{B.2}$$

The outer boundary is assumed to be closed

$$\frac{\partial p_{2D}}{\partial x}=0 \tag{B.3}$$

The mathematical model of outer area can be described using the Laplace transformations and dimensionless definitions

$$\begin{cases}\dfrac{\partial^2 \overline{p}_{2D}}{\partial x_D^2}-\dfrac{s}{\eta_{2D}}\overline{p}_{2D}=0\\ \overline{p}_{2D}(x_{1D})=\overline{p}_{eD}(x_{1D})\\ \left.\dfrac{\partial \overline{p}_{2D}}{\partial x_D}\right|_{x_D=x_{2D}}=0\end{cases} \tag{B.4}$$

The pressure solution to Eq. (B.4) is stated as

$$\begin{aligned}\overline{p}_{2D}(x_D)=&A_2\cosh\left((x_D-x_{2D})\sqrt{\frac{s}{\eta_{2D}}}\right)\\&+B_2\sinh\left((x_D-x_{2D})\sqrt{\frac{s}{\eta_{2D}}}\right)\end{aligned} \tag{B.5}$$

B_2 is 0 under the condition of constant pressure. The closed boundary condition of (B.4) allows for the determination of the coefficient A_2.

$$A_2=\frac{\overline{p}_{eD}(x_{1D})}{\cosh\left((x_{1D}-x_{2D})\sqrt{\frac{s}{\eta_{2D}}}\right)} \tag{B.6}$$

The pressure in the outer area can therefore be solved as

$$\overline{p}_{2D}(x_D)=\overline{p}_{eD}(x_{1D})\cdot\frac{\cosh\left((x_D-x_{2D})\sqrt{\frac{s}{\eta_{2D}}}\right)}{\cosh\left((x_{1D}-x_{2D})\sqrt{\frac{s}{\eta_{2D}}}\right)} \tag{B.7}$$

B.2 Closed-UPFs inner region

The closed-UPFs inner zone is divided by the closure of unpropped fracture in stimulated inner area with closed permeability k_e, the PDE of this closed-UPFs inner area is given by

$$\frac{\partial^2 \overline{p}_{eD}}{\partial x_D^2}-\frac{s}{\eta_{eD}}\overline{p}_{eD}=0 \tag{B.8}$$

At the interface of a closed-UPF inner area and the outer area

$$\frac{k_2}{\mu}\left.\frac{\partial \overline{p}_{2D}}{\partial x_D}\right|_{x_{1D}}=\frac{k_e}{\mu}\left.\frac{\overline{p}_{eD}}{\partial x_D}\right|_{x_{1D}} \tag{B.9}$$

The pressure solution to Eq. (B.8) can be written as

$$\begin{aligned}\overline{p}_{eD}(x_D)=&A_e\cosh\left((x_D-x_{1D})\sqrt{\frac{s}{\eta_{eD}}}\right)\\&+B_e\sinh\left((x_D-x_{1D})\sqrt{\frac{s}{\eta_{eD}}}\right)\end{aligned} \tag{B.10}$$

In Eq. (B.11), the coefficient A_e can be determined when x_D is equal to $x_{1D,}$ and then B_e can be obtained using Eq. (9).

$$A_e=\overline{p}_{eD}(x_{1D}) \tag{B.11}$$

$$B_e=\overline{p}_{eD}(x_{1D})c_1(s) \tag{B.12}$$

$$c_1(s)=\frac{k_2}{k_e}\sqrt{\frac{\eta_{eD}}{\eta_{2D}}}\cdot\tanh\left((x_{1D}-x_{2D})\sqrt{\frac{s}{\eta_{2D}}}\right) \tag{B.13}$$

Thus, the pressure solution to Eq. (B.10) is rewritten as

$$\overline{p}_{eD}(x_D)=\overline{p}_{eD}(x_{1D})\left(\cosh\left((x_D-x_{1D})\sqrt{\frac{s}{\eta_{eD}}}\right)+c_1(s)\sinh\left((x_D-x_{1D})\sqrt{\frac{s}{\eta_{eD}}}\right)\right) \tag{B.14}$$

B.3 Open-UPFs inner region

The closure of un-propped fracture causes the length of the stimulated inner area to shrink along the x-axis direction, and the original stimulated inner area gradually degenerates into a open-UPFs inner area. The inner zone of the open-UPFs maintains the same permeability as the original inner zone. The PDE of this open-UPFs inner area is expressed as

$$\frac{\partial^2 p_{dD}}{\partial x_D^2}-\frac{s}{\eta_{dD}}p_{dD}=0 \tag{B.15}$$

At the interface x_f of the open-UPFs and closed-UPFs inner area

$$\overline{p}_{dD}\left(x_{fD}\right)=\overline{p}_{eD}\left(x_{fD}\right) \tag{B.16}$$

$$\frac{k_d}{\mu}\frac{\partial\overline{p}_{dD}\left(x_{fD}\right)}{\partial x_D}=\frac{k_e}{\mu}\frac{\partial\overline{p}_{eD}\left(x_{fD}\right)}{\partial x_D} \tag{B.17}$$

Additionally, the interface between the open-UPFs inner region, the open-PFs, and the closed-PFs all exhibit continuous pressure.

$$\overline{p}_{dD}\left(\frac{w_D}{2}\right)=\overline{p}_{FD}\left(\frac{w_D}{2},\ 0<y_D<\sigma\right)=\overline{p}_{FCD}\left(\frac{w_D}{2},\ \sigma<y_D<1\right) \tag{B.18}$$

The pressure solution to Eq. (B.15) can be expressed as

$$\overline{p}_{dD}(x_D)=A_d\cosh\left(\left(x_D-x_{fD}\right)\sqrt{\frac{s}{\eta_{dD}}}\right)+B_d\sinh\left(\left(x_D-x_{fD}\right)\sqrt{\frac{s}{\eta_{dD}}}\right) \tag{B.19}$$

Combined with Eqs. (B.16) and (B.17), the coefficients A_d and B_d can be obtained

$$A_d=\overline{p}_{eD}(x_{1D})c_2(s) \tag{B.20}$$

$$B_d=\overline{p}_{eD}(x_{1D})c_3(s) \tag{B.21}$$

$$c_2(s)=\cosh\left(\left(x_{fD}-x_{1D}\right)\sqrt{\frac{s}{\eta_{eD}}}\right)+c_1(s)\sinh\left(\left(x_{fD}-x_{1D}\right)\sqrt{\frac{s}{\eta_{eD}}}\right) \tag{B.22}$$

$$c_3(s)=\frac{k_e}{k_d}\sqrt{\frac{\eta_{dD}}{\eta_{eD}}}\left(\sinh\left(\left(x_{fD}-x_{1D}\right)\sqrt{\frac{s}{\eta_{eD}}}\right)+c_1(s)\cosh\left(\left(x_{fD}-x_{1D}\right)\sqrt{\frac{s}{\eta_{eD}}}\right)\right) \tag{B.23}$$

Taking Eqs. (20) and (21) back to the general solution, we can rewrite Eq. (B.19)

$$\overline{p}_{dD}(x_D)=\overline{p}_{eD}(x_{1D})\left(c_2(s)\cosh\left(\left(x_D-x_{fD}\right)\sqrt{\frac{s}{\eta_{dD}}}\right)+c_3(s)\sinh\left(\left(x_D-x_{fD}\right)\sqrt{\frac{s}{\eta_{dD}}}\right)\right) \tag{B.24}$$

Combined with Eq. (B.18), the pressure solution of open-UPFs inner area can be rewritten as

$$\overline{p}_{dD}(x_D)=\frac{\overline{p}_{FCD}\left(\frac{w_D}{2},\sigma<y_D<1\right)}{c_4(s)}\left(c_2(s)\cosh\left(\left(x_D-x_{fD}\right)\sqrt{\frac{s}{\eta_{dD}}}\right)+c_3(s)\sinh\left(\left(x_D-x_{fD}\right)\sqrt{\frac{s}{\eta_{dD}}}\right)\right) \tag{B.25}$$

$$c_4(s)=c_2(s)\cosh\left(\left(\frac{w_D}{2}-x_{fD}\right)\sqrt{\frac{s}{\eta_{dD}}}\right)+c_3(s)\sinh\left(\left(\frac{w_D}{2}-x_{fD}\right)\sqrt{\frac{s}{\eta_{dD}}}\right) \tag{B.26}$$

B.4 Closed PFs region

In this work, the propped fracture is degraded to a closed zone of PFs with improved permeability. Given the transient flows from the open-UPFs inner area to the closed PFs area, the PDEs of the closed PFs zone can be written as

$$\frac{\partial^2\overline{p}_{FCD}}{\partial x_D^2}+\frac{\partial^2\overline{p}_{FCD}}{\partial y_D^2}-\frac{s}{\eta_{FCD}}\overline{p}_{FCD}=0 \tag{B.27}$$

At the interface between closed-PFs and open-PFs

$$\left.\frac{\partial\overline{p}_{FCD}}{\partial x_D}\right|_{x_D=0,y_D=\sigma}=0 \tag{B.28}$$

At the interface between open-UPFs inner zone and closed-PFs, the pressure and flow rate are continuous

$$\left.\frac{k_{FC}}{\mu}\frac{\partial\overline{p}_{FCD}}{\partial x_D}\right|_{x_D=w_D/2,\sigma<y_D<1}=\left.\frac{k_d}{\mu}\frac{\partial\overline{p}_{dD}}{\partial x_D}\right|_{x_D=w_D/2,\sigma<y_D<1} \tag{B.29}$$

$$\overline{p}_{FCD}(y_D=\sigma)=\overline{p}_{FD}(y_D=\sigma) \tag{B.30}$$

There is a closed boundary at the tip of propped fracture

$$\left.\frac{\partial\overline{p}_{FCD}}{\partial y_D}\right|_{y_D=1}=0 \tag{B.31}$$

Integrating Eq. (B.27) along the x direction, we can obtain

$$\int_0^{w_D/2}\frac{\partial^2\overline{p}_{FCD}}{\partial x_D^2}dx_D=\left.\frac{\partial\overline{p}_{FCD}}{\partial x_D}\right|_{w_D/2}-\left.\frac{\partial\overline{p}_{FCD}}{\partial x_D}\right|_0=\left.\frac{k_d}{k_{FC}}\frac{\partial\overline{p}_{dD}}{\partial x_D}\right|_{x_D=w_D/2,\sigma<y_D<1} \tag{B.32}$$

$$\int_0^{w_D/2}\left(\frac{\partial^2\overline{p}_{FCD}}{\partial y_D^2}-\frac{s}{\eta_{FCD}}\overline{p}_{FCD}\right)dx_D=\frac{w_D}{2}\left(\frac{\partial^2\overline{p}_{FCD}}{\partial y_D^2}-\frac{s}{\eta_{FCD}}\overline{p}_{FCD}\right) \tag{B.33}$$

Taking the boundary condition Eq. (B.28) into Eq. (B.27), it gives

$$\frac{\partial^2 \overline{p}_{FCD}}{\partial y_D^2} - c_6(s)\overline{p}_{FCD} = 0 \tag{B.34}$$

where c_6 is expressed as

$$c_6(s) = \frac{s}{\eta_{FCD}} - \frac{2}{C_{FCD}}c_5(s), \quad C_{FCD} = \frac{w_D k_{FC}}{k_d} \tag{B.35}$$

Therefore, the pressure solution to Eq. (B.34) is given by

$$\begin{aligned}\overline{p}_{FCD}(y_D) = A_{FCD}\cosh\left((y_D - 1)\sqrt{c_6(s)}\right) \\ + B_{FCD}\sinh\left((y_D - 1)\sqrt{c_6(s)}\right)\end{aligned} \tag{B.36}$$

With the combination of boundary condition Eqs. (B.29) and (B.33), the pressure in closed PFs region can be sloved

$$\overline{p}_{FCD}(y_D) = \frac{\overline{p}_{FD}(\sigma)}{\cosh\left((\sigma - 1)\sqrt{c_6(s)}\right)}\cosh\left((y_D - 1)\sqrt{c_6(s)}\right) \tag{B.37}$$

B.5 Open-PFs area

The fluid flow in open-PFs area can be described as

$$\frac{\partial^2 \overline{p}_{FD}}{\partial x_D^2} + \frac{\partial^2 \overline{p}_{FD}}{\partial y_D^2} - \frac{s}{\eta_{FD}}\overline{p}_{FD} = 0 \tag{B.38}$$

The constant-rate and pressure condition can be expressed as

$$\left.\frac{\partial \overline{p}_{FD}}{\partial y_D}\right|_{y_D=0} = -\frac{\pi}{C_{FD}\cdot s} \quad \text{(constant rate condition)} \tag{B.39}$$

$$\left.\frac{\partial \overline{p}_{FD}}{\partial y_D}\right|_{y_D=0} = -\frac{\pi}{C_{FD}}\overline{q}_{FD}, \quad \overline{p}_{FD}(y_D = 0) = \frac{1}{s} \quad \text{(constant pressure condition)} \tag{B.40}$$

Integrating Eq. (B.38) gives

$$\int_0^{w_D/2} \frac{\partial^2 \overline{p}_{FD}}{\partial x_D^2} dx_D = \left.\frac{\partial \overline{p}_{FD}}{\partial x_D}\right|_{w_D/2} - \left.\frac{\partial \overline{p}_{FD}}{\partial x_D}\right|_0 = \frac{k_d}{k_F}\left.\frac{\partial \overline{p}_{1D}}{\partial x_D}\right|_{x_D = w_D/2, 0 < y_D < \sigma} \tag{B.41}$$

$$\int_0^{w_D/2}\left(\frac{\partial^2 \overline{p}_{FD}}{\partial y_D^2} - \frac{s}{\eta_{FD}}\overline{p}_{FD}\right)dx_D = \frac{w_D}{2}\left(\frac{\partial^2 \overline{p}_{FD}}{\partial y_D^2} - \frac{s}{\eta_{FD}}\overline{p}_{FD}\right) \tag{B.42}$$

Eq. (B.39) can be rewritten as

$$\frac{k_d}{k_F}\left.\frac{\partial \overline{p}_{dD}}{\partial x_D}\right|_{x_D = w_D/2, 0 < y_D < \sigma} + \frac{w_D}{2}\left(\frac{\partial^2 \overline{p}_{FD}}{\partial y_D^2} - \frac{s}{\eta_{FD}}\overline{p}_{FD}\right) = 0 \tag{B.43}$$

It can be simplified as

$$\frac{\partial^2 \overline{p}_{FD}}{\partial y_D^2} - c_7(s)\overline{p}_{FD} = 0 \tag{B.44}$$

with

$$c_7(s) = \frac{s}{\eta_{FD}} - \frac{2}{C_{FD}}c_5(s) \tag{B.45}$$

$$C_{FD} = \frac{w_D k_F}{k_d} \tag{B.46}$$

The pressure solution to Eq. (B.43) is given by

$$\overline{p}_{FD}(y_D) = A_F\cosh\left((y_D - \sigma)\sqrt{c_7(s)}\right) + B_F\sinh\left((y_D - \sigma)\sqrt{c_7(s)}\right) \tag{B.47}$$

The coefficient B_F is obtained using Eq. (B.30)

$$\begin{aligned}B_F &= \frac{k_{FC}\overline{p}_{FD}(\sigma)\sqrt{c_6(s)}\tanh\left((\sigma - 1)\sqrt{c_6(s)}\right)}{k_F\sqrt{c_7(s)}} \\ &= \frac{A_F k_{FC}\sqrt{c_6(s)}\tanh\left((\sigma - 1)\sqrt{c_6(s)}\right)}{k_F\sqrt{c_7(s)}} = A_F c_8(s)\end{aligned} \tag{B.48}$$

with

$$c_8(s) = \frac{k_{FC}}{k_F\sqrt{c_7(s)}}\sqrt{c_6(s)}\tanh\left((\sigma - 1)\sqrt{c_6(s)}\right) \tag{B.49}$$

$$k_{FCD} = \frac{k_{FC}}{k_F} \tag{B.50}$$

Together with the constant rate condition, A_F can be determined

$$A_F = -\frac{\pi}{C_{FD}\cdot s c_9(s)} \tag{B.51}$$

Therefore, the bottomhole pressure is sloved and expressed as

$$\begin{aligned}\overline{p}_{wD} &= \overline{p}_{FD}(0) \\ &= \frac{\pi}{F_{CD}\cdot s c_9(s)}\left(c_8(s)\sinh\left(\sigma\sqrt{c_7(s)}\right) - \cosh\left(\sigma\sqrt{c_7(s)}\right)\right)\end{aligned} \tag{B.52}$$

If it is constant pressure, the coefficient A_F is given by

$$A_F = \frac{1}{s\left(\cosh\left(\sigma\sqrt{c_7(s)}\right) - c_8(s)\sinh\left(\sigma\sqrt{c_7(s)}\right)\right)} \tag{B.53}$$

The corresponding solution of flow rate is expressed as

$$\overline{q}_{FD} = -\frac{C_{FD}}{\pi}\sqrt{c_7(s)}\left(-A_F\sinh\left(\sigma\sqrt{c_7(s)}\right) + B_F\cosh\left(\sigma\sqrt{c_7(s)}\right)\right) \tag{B.54}$$

References

Abirifard, M., Birk, S., Raeisi, E., Sauter, M., 2022. Dynamic volume in karst aquifers: parameters affecting the accuracy of estimates from recession analysis. J. Hydrol. 128286. https://doi.org/10.1016/j.jhydrol.2022.128286.

Aybar, U., 2014. Investigation of Analytical Models Incorporating Geomechanical Effects on Production Performance of Hydraulically and Naturally Fractured Unconventional Reservoirs. MSc Thesis. The University of Texas at Austin, Austin, Texas.

Aybar, U., Eshkalak, M.O., Sepehrnoori, K., Patzek, T., 2014. Long term effect of natural fractures closure on gas production from unconventional reservoirs. In: SPE Eastern Regional Meeting. https://doi.org/10.2118/171010-MS.

Bello, R.O., 2009. Rate Transient Analysis in Shale Gas Reservoirs with Transient Linear Behavior. Doctor Dissertation. Texas A&M University.

Belytschko, T., Tabbara, M., 1996. Dynamic fracture using element free Galerkin methods. Int. J. Numer. Methods Eng. 39, 923–938.

Brown, M.L., 2009. Analytical trilinear pressure transient model for multiply fractured horizontal wells in tight shale reservoirs. 2000-2009-Mines Theses Diss.

MSc Thesis. The Colorado School of Mines.
Cao, C., Cheng, L., Jia, P., Shi, J., Dehghanpour, H., 2022. A dynamic fracture model combining with Laplace transform and synchronous iteration method for transient behavior analysis of a four-zone system. J. Hydrol. 615, 128723. https://doi.org/10.1016/j.jhydrol.2022.128723.
Cao, R., Shi, J., Jia, Z., Cao, C., Cheng, L., Liu, G., 2023. A modified 3D-EDFM method considering fracture width variation due to thermal stress and its application in enhanced geothermal system. J. Hydrol. 623, 129749. https://doi.org/10.1016/j.jhydrol.2023.129749.
Chipperfield, S.T., Wong, J.R., Warner, D.S., Cipolla, C.L., Mayerhofer, M.J., Lolon, E.P., Warpinski, N.R., 2007. Shear dilation diagnostics: a new approach for evaluating tight gas stimulation treatments. In: SPE Hydraulic Fracturing Technology Conference. https://doi.org/10.2118/106289-MS.
Cho, S.H., Kaneko, K., 2004. Influence of the applied pressure waveform on the dynamic fracture processes in rock. Int. J. Rock Mech. Min. Sci. 41, 771–784. https://doi.org/10.1016/j.ijrmms.2004.02.006.
Cho, Y., Apaydin, O.G.G., Ozkan, E., 2013. Pressure-dependent natural-fracture permeability in shale and its effect on shale-gas well production. SPE Reservoir Eval. Eng. 16, 216–228. https://doi.org/10.2118/159801-PA.
Cinco, L.H., Samaniego, V.F., Dominguez, A.N., 1978. Transient pressure behavior for a well with a finite-conductivity vertical fracture. SPE J. 18, 253–264. https://doi.org/10.2118/6014-PA.
Dahi-Taleghani, A., 2011. Numerical modeling of multistranded- hydraulic-fracture propagation: accounting for the interaction between induced and natural fractures. SPE J. 16 (3), 575–581. https://doi.org/10.2118/124884-PA.
Di, S., Cheng, S., Wei, C., Shi, W., Wang, Y., 2021. Evaluation of fracture closure and its contribution to total production for a well with non-planar asymmetrical vertical fracture based on bottom-hole pressure. J. Pet. Sci. Eng. 205, 108864. https://doi.org/10.1016/j.petrol.2021.108864.
El-Banbi, A.H., 1998. Analysis of Tight Gas Well Performance. Doctor Dissertation. Texas. A & M University.
Fabbri, H.A., Cleto, P.R., Gaiotto, A.T., Rodrigues, E.A., Maedo, M.A., Manzoli, O.L., 2021. Modeling the closure behavior of natural fractures in porous media using high aspect ratio interface elements. J. Pet. Sci. Eng. 196, 107979. https://doi.org/10.1016/j.petrol.2020.107979.
Gaddipati, M., Karacaer, C., Ozgen, C., Firincioglu, T., Bowen, G., Pallister, I., Shaw, G., 2020. Overcoming the limitations of SRV concept. In: SPE/AAPG/SEG Unconventional Resources Technology Conference. https://doi.org/10.15530/urtec-2020-3221.
Gupta, A., Krishnan, U.M., Mandal, T.K., Chowdhury, R., Nguyen, V.P., 2022. An adaptive mesh refinement algorithm for phase-field fracture models: application to brittle, cohesive, and dynamic fracture. Comput. Methods Appl. Mech. Eng. 399, 115347. https://doi.org/10.1016/j.cma.2022.115347.
Hernandez, R.F., Younes, A., Fahs, M., Hoteit, H., 2023. Pressure transient analysis for stress-sensitive fractured wells with fracture face damage. Geoenergy Sci. Eng. 221, 211406. https://doi.org/10.1016/j.geoen.2022.211406.
Ji, L., Sen, V., Min, K.S., Sullivan, R., 2019. Numerical simulation of DFITs within a coupled reservoir flow and geomechanical simulator - insights into completions optimization. In: SPE Hydraulic Fracturing Technology Conference and Exhibition. https://doi.org/10.2118/194352-MS.
Ji, L., Settari, A.T., Sen, V., Sullivan, R., Puchyr, P., 2020. Comprehensive simulation of hydraulic fracturing through mechanical stratigraphy with explicit width calculation and leakoff: foundations of completion modeling. In: SPE Hydraulic Fracturing Technology Conference and Exhibition. https://doi.org/10.2118/199692-MS.
Jia, P., Ma, M., Cheng, L., Clarkson, C.R., 2020. A semi-analytical model for capturing dynamic behavior of hydraulic fractures during flowback period in tight oil reservoir. Energy Sci. Eng. 8, 3415–3440. https://doi.org/10.1002/ese3.769.
Jia, P., Ma, M., Cao, C., Cheng, L., Yin, H., Li, Z., 2022. Capturing dynamic behavior of propped and unpropped fractures during flowback and early-time production of shale gas wells using a novel flow-geomechanics coupled model. J. Pet. Sci. Eng. 208, 109412. https://doi.org/10.1016/j.petrol.2021.109412.
Jia, Z., Cheng, L., Feng, H., Cao, R., Jia, P., Pu, B., Pan, Q., Shi, J., 2023. Full composition numerical simulation of CO_2 utilization process in shale reservoir using projection-based embedded discrete fracture model (pEDFM) considering nano-confinement effect. Gas Sci. Eng. 111, 204932. https://doi.org/10.1016/j.jgsce.2023.204932.
Juanes, R., Spiteri, E.J., Orr, Jr.F.M., Blunt, M.J., 2006. Impact of relative permeability hysteresis on geological CO_2 storage. Water Resour. Res. 42. https://doi.org/10.1029/2005WR004806.
Kamali, A., Ghassemi, A., 2019. DFIT considering complex interactions of hydraulic and natural fractures. In: SPE Hydraulic Fracturing Technology Conference and Exhibition. https://doi.org/10.2118/194348-MS.
Karma, A., Kessler, D.A., Levine, H., 2001. Phase-field model of mode iii dynamic fracture. Phys. Rev. Lett. 87, 045501. https://doi.org/10.1103/PhysRevLett.87.045501.
Lamidi Benson, A.-L., Clarkson, C.R., 2023. A semi-analytical flowback data history-matching approach that rigorously accounts for fracture dynamics. Geoenergy Sci. Eng. 231, 212289. https://doi.org/10.1016/j.geoen.2023.212289.
Li, Y., Dai, F., Liu, Y., Wei, M., 2022. Experimental evaluation of the transient propagation fracture properties of rocks under dynamic mode I loading: an insight from digital image correlation. Theor. Appl. Fract. Mech. 119, 103370. https://doi.org/10.1016/j.tafmec.2022.103370.
Lin, R., Ren, L., Zhao, J., Wu, L., Li, Y., 2017. Cluster spacing optimization of multi-stage fracturing in horizontal shale gas wells based on stimulated reservoir volume evaluation. Arabian J. Geosci. 10, 38. https://doi.org/10.1007/s12517-016-2823-x.
Liu, Y., Leung, J.Y., Chalaturnyk, R., 2018. Geomechanical simulation of partially propped fracture closure and its implication for water flowback and gas production. SPE Reservoir Eval. Eng. 21, 273–290. https://doi.org/10.2118/189454-PA.
Luo, L., Cheng, S., Lee, J., 2021. Time-normalized conductivity concept for analytical characterization of dynamic-conductivity hydraulic fractures through pressure-transient analysis in tight gas reservoirs. J. Nat. Gas Sci. Eng. 92, 103997. https://doi.org/10.1016/j.jngse.2021.103997.
Mittal, R., Oruganti, Y., McBurney, C., 2015. Re-fracturing simulations: pressure-dependent SRV and shear dilation of natural fractures. In: SPE/AAPG/SEG Unconventional Resources Technology Conference. https://doi.org/10.15530/URTEC-2015-2154943.
Moradi, P.M., Angus, D., 2019. Modeling frac-hits using dynamic microseismicity-constrained enhanced fracture regions. In: SPE/AAPG/SEG Unconventional Resources Technology Conference. https://doi.org/10.15530/urtec-2019-258.
Moussa, T., Dehghanpour, H., Fu, Y., Ezulike, O., 2020. The use of flowback data for estimating dynamic fracture volume and its correlation with completion-design parameters: eagle Ford cases. J. Pet. Sci. Eng. 195, 107584. https://doi.org/10.1016/j.petrol.2020.107584.
Mustafa, A., Tariq, Z., Abdulraheem, A., Mahmoud, M., Al Nakhli, A., BaTaweel, M., 2018. Increasing stimulated reservoir volume srv in unconventional reservoirs: microstructural and rock mechanical study. In: Abu Dhabi International Petroleum Exhibition & Conference. https://doi.org/10.2118/192808-MS.
Panahi, M., Rahmati, O., Kalantari, Z., Darabi, H., Rezaie, F., Moghaddam, D.D., Ferreira, C.S.S., Foody, G., Aliramaee, R., Bateni, S.M., Lee, C.-W., Lee, S., 2022. Large-scale dynamic flood monitoring in an arid-zone floodplain using SAR data and hybrid machine-learning models. J. Hydrol. 611, 128001. https://doi.org/10.1016/j.jhydrol.2022.128001.
Pettersson, K., Maggiolo, D., Sasic, S., Johansson, P., Sasic Kalagasidis, A., 2021. Contribution of dynamic capillary pressure to rainfall infiltration in thin homogeneous growth substrates. J. Hydrol. 603, 126851. https://doi.org/10.1016/j.jhydrol.2021.126851Pinzon.
Pinzon, C.L., Chen, H.-Y., Teufel, L.W., 2000. Complexity of well testing analysis of naturally-fractured gas-condensate wells in Colombia. In: SPE International Petroleum Conference and Exhibition. https://doi.org/10.2118/59013-MS.
Ren, L., Lin, R., Zhao, Jinzhou, Rasouli, V., Zhao, Jiangyu, Yang, H., 2018. Stimulated reservoir volume estimation for shale gas fracturing: mechanism and modeling approach. J. Pet. Sci. Eng. 166, 290–304. https://doi.org/10.1016/j.petrol.2018.03.041.
Ren, L., Su, Y., Zhan, S., Meng, F., Zhao, G., 2019. Fully coupled fluid-solid numerical simulation of stimulated reservoir volume (SRV)-fractured horizontal well with multi-porosity media in tight oil reservoirs. J. Pet. Sci. Eng. 174, 757–775. https://doi.org/10.1016/j.petrol.2018.11.080.
Roussel, N.P., Agrawal, S., 2017. Introduction to poroelastic response analysis—quantifying hydraulic fracture geometry and SRV permeability from offset-well pressure data. In: The 5th Unconventional Resources Technology Conference. https://doi.org/10.15530/urtec-2017-2645414.
Sarna, A., Xing, Q., Mork, J., Ershaghi, I., 2014. Impact of fracture closure on productivity decline of unconventional wells. In: SPE Western North American and Rocky Mountain Joint Meeting. https://doi.org/10.2118/169590-MS.
Sen, V., Min, K.S., Ji, L., Sullivan, R., 2018. Completions and well spacing optimization by dynamic SRV modeling for multi-stage hydraulic fracturing. In: SPE Annual Technical Conference and Exhibition. https://doi.org/10.2118/191571-MS.
Seth, P., Kumar, A., Manchanda, R., Shrivastava, K., Sharma, M.M., 2018. Hydraulic fracture closure in a poroelastic medium and its implications on productivity. In: The 52nd US Rock Mechanics/Geomechanics Symposium.
Shi, J., Cheng, L., Cao, R., Fang, J., Yang, C., Liu, G., Du, X., 2023. Analysis and quantitative evaluation of temperature influence mechanism of multi-cycle water huff-n-puff in ultra-low permeability reservoirs. Energy 263, 125600. https://doi.org/10.1016/j.energy.2022.125600.
Stalgorova, E., Mattar, L., 2013. Analytical model for unconventional multifractured composite systems. SPE Reservoir Eval. Eng. 16, 246–256. https://doi.org/10.2118/162516-PA.
Swami, V., Settari, A., Sahai, R., Costello, D., Mercer, A., 2017. A novel approach to history matching and optimization of shale completions and EUR—a case study of eagle ford well. In: SPE Unconventional Resources Conference. https://doi.org/10.2118/185075-MS.
Vairogs, J., Hearn, C.L., Dareing, D.W., Rhoades, V.W., 1971. Effect of rock stress on gas production from low-permeability reservoirs. J. Petrol. Technol. 23, 1161–1167. https://doi.org/10.2118/3001-PA.
van den Hoek, P.J., 2003. A novel methodology to derive the dimensions and degree of containment of waterflood-induced fractures from pressure transient analysis. In: SPE Annual Technical Conference and Exhibition. https://doi.org/10.2118/84289-MS.
Wang, H., Yi, S., Sharma, M.M., 2018. A computationally efficient approach to modeling contact problems and fracture closure using superposition method. Theor. Appl. Fract. Mech. 93, 276–287. https://doi.org/10.1016/j.tafmec.2017.09.009.
Wang, Y., Cheng, S., Zhang, K., Ayala, L.F., 2019. Investigation on the transient pressure response of water injector coupling the dynamic flow behaviors in the wellbore, waterflood-induced fracture and reservoir: semi-analytical modeling and a field case. Int. J. Heat Mass Tran. 130, 668–679. https://doi.org/10.1016/j.ijheatmasstransfer.2018.09.083.

Wang, K., Tang, C., Li, G., Lu, Z., 2022. Numerical simulation of dynamic fractures in 2D FGMs using the numerical manifold method. Eng. Anal. Bound. Elem. 140, 32–47. https://doi.org/10.1016/j.enganabound.2022.04.002.

Wang, Q., Zhao, J., Wang, B., Li, D., Ran, L., Hu, Y., Zhao, C., 2022. Secondary growth and closure behavior of planar hydraulic fractures during shut-in. J. Pet. Sci. Eng. 213, 110420. https://doi.org/10.1016/j.petrol.2022.110420.

Wu, D., Yu, L., Ju, M., Li, S., Liu, R., Su, H., Zhou, L., 2022. Study on the mode I fracture properties of granites after heating and water-cooling treatments under different impact loadings. Rock Mech. Rock Eng. 55, 4271–4290. https://doi.org/10.1007/s00603-022-02865-0.

Yuan, B., Su, Y., Moghanloo, R.G., Rui, Z., Wang, W., Shang, Y., 2015. A new analytical multi-linear solution for gas flow toward fractured horizontal wells with different fracture intensity. J. Nat. Gas Sci. Eng. 23, 227–238. https://doi.org/10.1016/j.jngse.2015.01.045.